2. Scaling mass transport of nanoconfined water

2.1. Introduction to nanoconfined water

Despite its fundamental importance in science and technology, the physical and transport properties of water are far from being completely understood [17]. The self-diffusion of water molecules D in proximity of solid surfaces, at the interface between immiscible liquids, and in confined geometries, such as nanopores and nanotubes, is a very different process as compared to the bulk phase [33, 42, 88–90]. The thermal agitation of the water molecules in the bulk liquid is only dictated by the local temperature and pressure conditions, and molecular diffusion follows the Einstein relation [16]. Differently, under confined conditions, the mobility of water molecules is perturbed by the presence of additional interaction forces arising at the water/solid interfaces, mainly van der Waals and Coulomb interactions. These additional forces usually reduce the local molecular diffusion [91, 92]. Even if considerable work has been done in recent years, both experimentally and theoretically, to understand and characterize the perturbed behavior of the water molecules in confined geometries, there is still no complete comprehension of the process and often the published results are contradictory [93].

Controlling the mobility of water molecules is of relevance to several scientific disciplines and has implications in multiple technological applications. For instance, water adsorption/desorption in nanoporous materials, such as zeolites, has potential in long-term thermal storage and energy engineering [6, 94]; filters with nanopores and nanochannels are increasingly explored for their large surface area and higher efficiency [95, 96]; in heat transfer problems, nanofluids are under investigation because of their peculiar thermal properties [97, 98]; in micro/nanotechnology processes, controlling the deposition and surface diffusion of water molecules is critical for precise manufacturing [99, 100]; in biology, the mechanisms regulating

the transport of single water molecules through cell membrane channels (aquaporins) and the multiscale water compartmentalization in tissues are still elusive [101–105]. Also, proteins tend to modify their structure and function according to the surrounding aqueous environment [106–108]. Finally, nanomedicine is one of the fields which can take more advantage from the anomalous behavior of nanoconfined water, especially for designing novel Magnetic Resonance Imaging (MRI) contrast agents (see Chapter 6 for a detailed discussion) or drug delivery technologies.

In this Chapter, the self-diffusion coefficient of water molecules is investigated through Molecular Dynamics (MD) simulations under five different isothermal configurations, namely within silica nanopores; around spherical hydroxylated nanoparticles (NPs); within silica nanopores filled by NPs; in the proximity of single-wall carbon nanotubes (CNTs) and proteins. The self-diffusion coefficient for all different configurations has been found to scale with a single non-dimensional parameter θ, incorporating both geometrical and physicochemical information, following the relationship $D(\theta) = D_B[1 + (D_C/D_B - 1)\theta]$. The $D(\theta)$ scaling is modulated by the coefficients D_B and D_C, which represent the bulk and totally confined diffusion of water, respectively. This law would help in explaining and rationalizing previous experimental evidences [14], and represents a ready-to-use tool for the rational design of nanoconstructs based on the nanoscale confinement of water molecules.

2.2. Molecular Dynamics methods

The coefficient D of water under nanoconfined conditions is estimated by molecular dynamics simulations for almost 60 cases, by varying the size of the nanoparticles and nanopores, the electrostatic surface charges and level of hydrophobicity, as well as the type of protein. In this Section, the considered MD methods (geometries, force fields and simulation protocols) are detailed [27].

2.2.1. Geometries

MD simulations are used to compute the self-diffusion coefficient D of water molecules confined under different configurations. These are briefly summarized in Figure 2.1 and include the case of water molecules (blue dots) moving (a) around spherical hydroxylated nanoparticles (NPs) (gray

dots); (b) within a hydrated nanopore (gray dots); around (c) hydroxylated NPs (red dots) adsorbed on the surface of a hydrated nanopore (gray dots); (d), around and within single-walled carbon nanotubes (CNTs); and (e-f) around proteins. The NPs are made out of magnetite (Fe_3O_4) crystals (red and cyan dots), with OH^- functional groups on their surface; or silica (SiO_2) crystals (gray dots), with silanol SiOH functional groups on the surface. The nanopores are made out of silica only. Hereafter, a detailed description of the simulated geometries is provided.

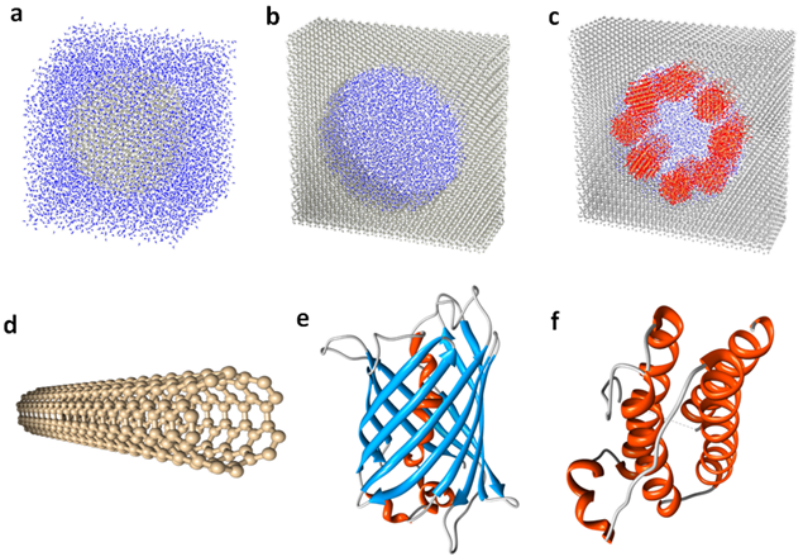

Figure 2.1.: Some of the analyzed configurations. (a) Silica particle in water, diameter $\phi = 5.2$ nm (blue dots: water molecules; gray dots: silica atoms); (b) silica nanopore filled by water, diameter $\Phi = 8.1$ nm; (c) 16 magnetite nanoparticles within a silica nanopore filled by water, $\phi = 2.0$ nm and $\Phi = 8.1$ nm (red and cyan dots: magnetite atoms); (d) single-walled carbon nanotube with chirality (5,5); (e) Green Fluorescence protein; (f) Leptin protein (the standard ribbon visualization of secondary structures has been used for proteins). In (d,e,f) water molecules have been removed for clarity. Figure adapted from Reference [27].

Nanopores and nanoparticles

A first set of geometries analyzed by MD simulations are cylindrical nanopores and spherical nanoparticles (NPs). Nanopores are made out of silica; NPs are made out of magnetite or silica.

First, a unit cell of alpha-quartz (SiO_2) [109] (leftmost picture of Figure 2.2) is considered. The latter unit cell is replicated along all Cartesian axes, such that a fully periodic brick with size 11.30 x 11.06 x 4.32 nm^3 is constructed (middle picture in Figure 2.2). A computational domain with smaller dimensions compared to typical experiments is considered [14], for reducing the computational demand. However, this is not a restricting hypothesis as proved by the good scalability of the results in terms of the presented parameter θ. Subsequently, a nanopore in the above brick is obtained by removing all atoms whose distance from the brick center is smaller than a fixed length (i.e. nanopore radius). For the sake of simplicity, since here the main concern is to investigate on the trend of the self-diffusion coefficient of water molecules in different nanoconfined conditions, here amorphization of silica is neglected.

Upon the creation of the pore (see the rightmost picture in Figure 2.2), all silicon atoms located along the "cut surface" with only one bonded oxygen atom are removed. In addition, one hydrogen atom is attached to all oxygen atoms that are missing one bond with silicon (surface oxygen). This is achieved by imposing that the angle formed by silicon, oxygen and hydrogen is 128.8 degrees (elevation) [110], with a random azimuth angle (see Figure 2.4a).

A unit cell of magnetite (Fe_3O_4) [111] (leftmost picture of Figure 2.3) is then considered. The latter unit cell is replicated along all Cartesian axes, such that a fully periodic brick with desired size is constructed (e.g. 3.0 x 3.0 x 3.0 nm^3 in the middle picture in Figure 2.3). Finally, a spherical particle is obtained by retaining only atoms within a fixed distance from the brick center (radius), as shown in the rightmost picture of Figure 2.3.

After the above cut, the NP surface is treated by the following procedure: 1) Iron atoms Fe^{2+} and Fe^{3+} are removed when they have less than 4 and 6 bonds, respectively; 2) a bonded hydrogen atom is attached to all oxygen atoms with only one bond at the magnetite surface. The Fe-O-H angle can be estimated between 125° (DFT, quantum) and 128° (SPASIBA, empirical force field) for Fe^{2+}; while this Fe-O-H angle can be estimated between 126° (DFT, quantum) and 130° (SPASIBA, empirical force field) for Fe^{3+} [112]. In the simulations, it has been found that the numerical results are

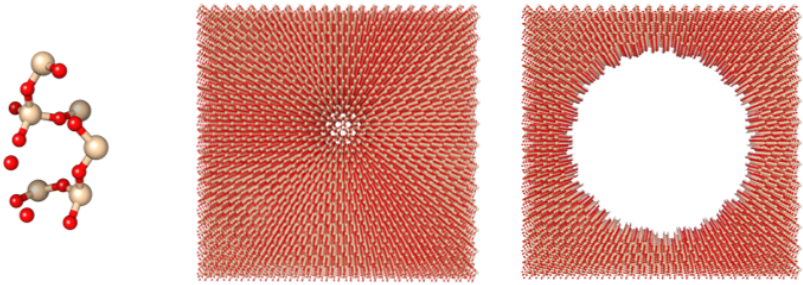

Figure 2.2.: Preparation of the MD geometry of a silica nanopore. From left to right: unit cell of alpha-quartz; silica crystal brick (11.30 x 11.06 x 4.32 nm^3); silica pore (8 nm diameter), before surface functionalization.

not very sensitive to this angle and hence the same angle of the silanol group (129°) is used in the geometry preparation for the sake of simplicity, with a random azimuth angle (see Figure 2.4b). Such an approach of modeling the surface aims at mimicking real SPIO particles without coating [113], and it represents a simple technique already validated in other works for iron nanoparticles in aqueous environment [114]. On the other hand, here the effect due to complex coatings will be indirectly taken into account by a sensitivity analysis of the nonbonded interactions (Lennard-Jones and partial charges parameterizations).

Towards the end of minimizing the effects due to the residual electrical dipole induced by the charges located at the NPs surface, in all the studied setups NPs are inserted in pairs within the nanopore, where the first particle (which undergoes a random rigid rotation on each Cartesian axis) is initially opposed to its mirror image with respect to the midpoint of the line segment connecting the centers of the two particles (see Figure 2.5). In the initial configuration of the simulations, all NPs pairs have the latter segment parallel to the pore axis.

Proteins

The second set of geometries analyzed by MD simulations aims to study the effect of different proteins on the mass transfer properties of the surrounding water molecules. Proteins are biological macromolecules made of one

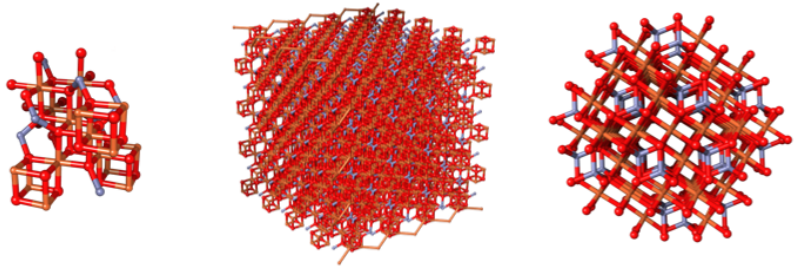

Figure 2.3.: Preparation of the MD geometry of a magnetite nanoparticle. From left to right: unit cell of magnetite; magnetite crystal brick (3.0 x 3.0 x 3.0 nm^3); magnetite nanoparticle (2 nm diameter), before surface functionalization.

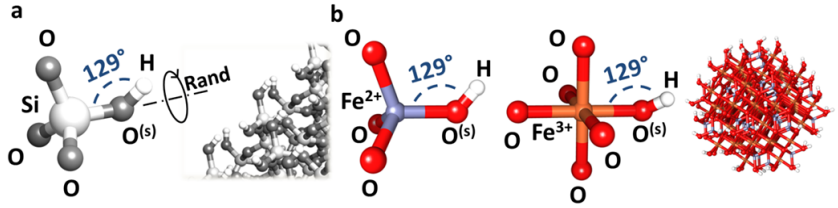

Figure 2.4.: Silica and magnetite surface functionalization. (a) Silica tetrahedron with geometric details of silanol surface group and magnification of a silica surface. The dihedral angle O-Si-$O^{(s)}$-H is randomly chosen, where $O^{(s)}$ is the oxygen atom belonging to silanol; (b) Fe^{2+} tetrahedron and Fe^{3+} octahedron within magnetite crystals, with details of the Fe^{2+}OH and Fe^{3+}OH surface groups. A magnetite particle (ϕ = 2.0 nm) with functionalized surface is shown in the rightmost part.

or more chains of amino acids, performing a vast variety of functions within living organisms. Amino acids show hydrophilic or hydrophobic character according to the structure and polarity of their residues. As a matter of facts, proteins may modify their structure and thus their functionality according to the dynamics of surrounding water environment [107, 115, 116]. Dense protein products, such as pharmaceutical preparations or high protein nutrition bars, involve ongoing challenges for controlling the viscosity of the water-protein system and for reducing protein self-association

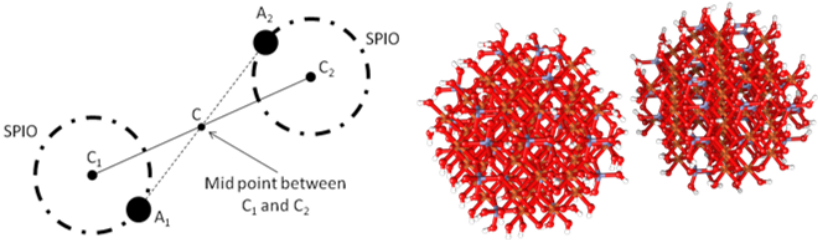

Figure 2.5.: Relative positions of NPs couples. NPs are constructed in pairs where each particle represents the mirror image of the other with respect to the midpoint of the line segment connecting the centers of the two particles (on the left-hand side, atom A_1 is the mirror image of A_2 with respect to C). On the right-hand side a rendered image of a SPIO mirrored pair is shown.

phenomena [117]; enzymatic activity, molecular recognition and folding process of proteins are strongly influenced by surrounding water mobility and hydration [118]; fluctuations between different conformational substates, which are determined by local temperature and minima of potential energy surface and are related to the biological function of the proteins [119], are influenced by the hydrogen bond creation/destruction at the solvent-protein interface and thus by surrounding water dynamics [106, 120–122].

Numerous experimental and theoretical studies have already demonstrated that the water molecules in the proximity of a protein surface are subjected to confined dynamics, i.e. a general decrease in the self-diffusion coefficient respect to the bulk value and a substantial modification of the actual solvent structure [123–125]. Water diffusion has been studied both locally (i.e. by considering the water diffusion in the proximity of spatial uniform sub-regions of proteins) and globally (i.e. by evaluating the spatially averaged water diffusion as a function of the distance from protein surface) [118]. However, a general modelling and broad physical understanding of the water mobility modification in the vicinity of any protein is still a subject of investigation, mainly because of the variety of physicochemical properties (hydrophilic vs. hydrophobic) of the few tens of amino acids or functional groups being the building blocks of millions of known

proteins.

Hence, a wide range of solvated proteins is here considered, in order to systematically study their effect on the surrounding water dynamics. First, a simple B1-Immunoglobulin binding domain of streptococcal Protein G (1PGB entry in the Protein Data Bank [126]), which is involved in the bonding process between many infectious bacteria and host immunoglobulins and currently used in many biomedical applications, is considered (Figure 2.6). B1-Immunoglobulin binding domain is solvated in SPC/E water boxes with different sizes, ranging from 348 nm^3 (11253 water molecules) to 23 nm^3 (496 water molecules), but similar water density ($\cong$ 1000 kg m^{-3}).

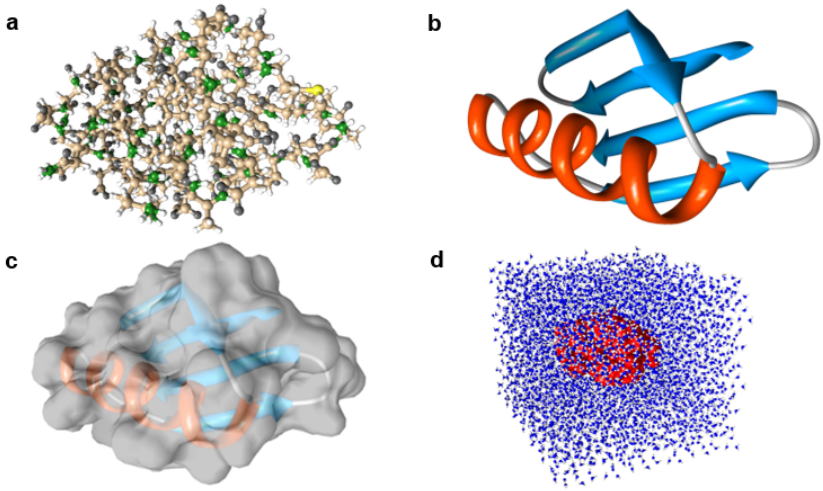

Figure 2.6.: MD geometry of B1-Immunoglobulin binding domain. (a) Atomistic visualization. (b) Ribbon visualization of secondary structures (orange for alpha-helices; cyan for beta-sheets; gray for random coils). (c) Solvent accessible surface of the protein (light gray). (d) Protein (red) solvated in SPC/E water box (blue).

Second, ubiquitin (1UBQ [127]), which is a small and globular regulatory protein found in almost all tissues of eukaryotic organisms, is considered (Figure 2.7a). Ubiquitin is again solvated in SPC/E water boxes with

different sizes, ranging from 817 nm^3 (26758 water molecules) to 60 nm^3 (1554 water molecules), but similar water density ($\cong$ 1000 kg m^{-3}).

Finally, six more proteins, with a vast array of geometries, sizes and functions within living organisms, are also solvated at similar water density ($\cong$ 1000 kg m^{-3}) and studied by MD simulations: Glucokinase (1V4S [128], Figure 2.7b), which is an enzyme involved in the regulation of carbohydrate metabolism by acting as a glucose sensor, solvated in a 580 nm^3 SPC/E water box (16864 water molecules); Green fluorescence protein (1QXT [129], Figure 2.7c), which is a fluorescent protein of many marine organisms widely used in fluorescence microscopy technique, solvated in a 348 nm^3 SPC/E water box (10353 water molecules); Leptin (1AX8 [130], Figure 2.7d), which is a human hormone regulating many metabolism-related behaviors such as appetite and hunger, solvated in a 348 nm^3 SPC/E water box (10878 water molecules); Lysozyme (1AKI [131], Figure 2.7e), which is an enzyme part of the innate immune system, solvated in a 348 nm^3 SPC/E water box (10882 water molecules); Myoglobin (1MBS [132], Figure 2.7f), which is found in the muscle tissue of vertebrates for oxygen transport, solvated in a 348 nm^3 SPC/E water box (10743 water molecules); Ca^{2+}-ATPase (1KJU [133], Figure 2.7g), which is a P-type ion pump for transporting Ca^{2+} across the cellular membrane, solvated in a 1215 nm^3 SPC/E water box (35426 water molecules). The simulated conformation of Ca^{2+}-ATPase corresponds to the Ca^{2+}-free (E2) state. As noticeable in Figure 2.7, the geometry of simulated proteins ranges from almost spherical (e.g. ubiquitin) to elongated (e.g. Ca^{2+}-ATPase) shapes, from small (e.g. 562 atoms of B-Immunoglobulin binding domain) to larger sizes (e.g. 9667 atoms of Ca^{2+}-ATPase); whereas the biological function spans from catalytic (e.g. Glucokinase) to hormonal (e.g. Leptin) or transport proteins (e.g. Myoglobin).

Note that crystal water molecules are removed from original PDB files, in order to fully solvate the protein by means of the GROMACS's tool *genbox*.

Carbon nanotubes

The last set of geometries analyzed by MD simulations aims to evaluate the diffusion of water in the proximity of strongly hydrophobic surfaces, such as carbon nanotube (CNT) ones. CNTs have been recognized as promising building blocks of novel nanostructured materials, because of

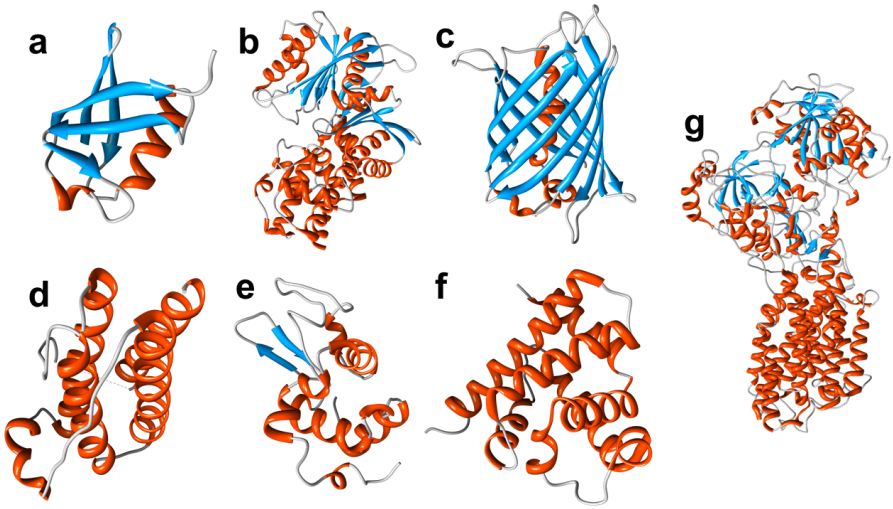

Figure 2.7.: Secondary structures (orange for alpha-helices; cyan for beta-sheets; gray for random coils) of the simulated proteins are displayed. (a) Ubiquitin. (b) Glucokinase. (c) Green Fluorescence. (d) Leptin. (e) Lysozyme. (f) Myoglobin. (g) Ca^{2+}-ATPase.

their exceptional mechanical, thermal and electrical features [134]. Mechanical, thermal and electrical properties of CNTs are well documented in the literature [134, 135]; in contrast, even if CNT-based porous materials may be interesting components of nanofluidic devices for biomedical applications [136–138], the physical understanding of transport properties of fluids through or around their pores is still incomplete, because of the difficulty in setting up adequate experimental setups [139]. Nevertheless, computational studies have already demonstrated a general reduction of water mobility both within (e.g. Figure 2.8b) and around CNTs (e.g. Figure 2.8c), or close to graphene surfaces, according to different pore size, surface functionalization or hydration level of these carbon structures [139].

Here, armchair CNTs with different chirality (i.e. diameter) are solvated in triclinic SPC/E water boxes with different volumes, in order to evaluate the geometry effect on the overall self-diffusion coefficient of water. First, a (5,5) CNT (i.e. 0.7 nm diameter) 5 nm long (Figure 2.8a) is solvated in

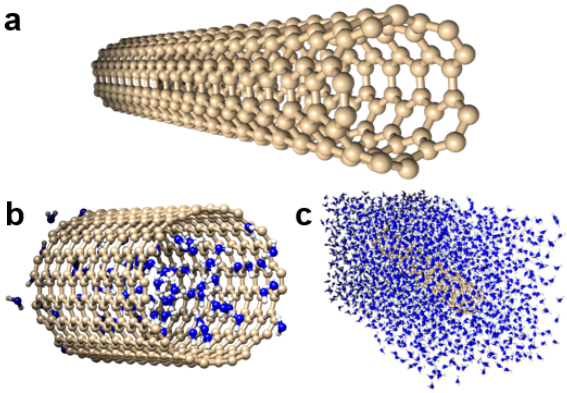

Figure 2.8.: MD geometries of solvated carbon nanotubes (CNTs). (a) (5,5) CNT 5 nm long. (b) (10,10) CNT filled by water. (c) (5,5) CNT 5 nm long solvated in a water box.

water boxes ranging from 15 (317 water molecules) to 316 (10023 water molecules) nm^3 (Figure 2.8c). Then, 10 nm long (10,10) CNT (i.e. 1.4 nm diameter), (20,20) CNT (i.e. 2.7 nm diameter) and (30,30) CNT (i.e. 4.1 nm diameter) are solvated in 132 (3689 water molecules), 260 (7284 water molecules) and 431 (12351 water molecules) nm^3 SPC/E water boxes, respectively. Notice that water density is $\cong$ 1000 kg m^{-3} in all simulated CNT setups, which corresponds to fully hydrated CNT surfaces. Carbon nanotubes geometries are generated by means of the VMD – Visual Molecular Dynamics software [140].

2.2.2. Force field

Two types of interactions are considered in the MD simulations: i) bonded interactions, among the atoms forming nanopores, nanoparticles, CNTs or proteins; ii) nonbonded interactions, between the water molecules and the solid surfaces, described via van der Waals and Coulomb potentials.

First, bonded and nonbonded interactions of proteins are modeled using the GROMOS96 43a2 force field [141], which has been widely used for studying water dynamics in the proximity of protein surfaces [142, 143].

Second, in the silica structure, the bonded interactions are modeled by means of two harmonic terms, adopted to describe the silicon-oxygen and oxygen-hydrogen interactions. That is, a bond stretching potential between two bonded atoms i and j at a distance r_{ij} (around the equilibrium distance r_{ij}^0), and a bending angle potential between the two pairs of bonded atoms (i,j) and (j,k) (around the equilibrium angle ϑ_{ijk}^0) are considered as follows:

$$U_{BOND}\left(r_{ij},\vartheta_{ijk}\right)=\frac{1}{2}k_{ij}^{b}\left(r_{ij}-r_{ij}^{0}\right)^{2}+\frac{1}{2}k_{ijk}^{\vartheta}\left(\vartheta_{ijk}-\vartheta_{ijk}^{0}\right)^{2}, \tag{2.1}$$

with parameters reported elsewhere [144].

In the magnetite structure, sufficiently high values for the force constants in Equation 2.1 are assumed for all bonded interactions (rigid particle assumption), namely $k_{ij}^b = 400000$ kJ mol^{-1} nm^{-2} and $k_{ijk}^{\vartheta} = 400$ kJ mol^{-1} rad^{-2}. In fact, here the main concern is to investigate water self-diffusion coefficient of water in nanoconfined geometries, which is affected by nonbonded interactions. Therefore, here it is not of interest to accurately describe the fast dynamics within the magnetite NPs, thus the rigid particle assumption does not affect the measurements of self-diffusion coefficient of water, as confirmed by preliminary sensitivity analyses with respect to k_{ij}^b and k_{ijk}^{ϑ} (results not shown).

In the CNT structure, the carbon-carbon bonded interactions are also modeled by two harmonic terms (Equation 2.1), where $k_{ij}^b = 478900$ kJ mol^{-1} nm^{-2}, $r_{ij}^0 = 0.142$ nm, $k_{ijk}^{\vartheta} = 562.2$ kJ mol^{-1} rad^{-2}and $\vartheta_{ijk}^0 = 120°$ [145–147].

Nonbonded interactions among silica atoms (consisting in both van der Waals and electrostatic interactions) are also taken into account through: (i) a Lennard-Jones term

$$U_{LJ}\left(r_{ij}\right)=4\varepsilon_{ij}\left[\left(\frac{\sigma_{ij}}{r_{ij}}\right)^{12}-\left(\frac{\sigma_{ij}}{r_{ij}}\right)^{6}\right], \tag{2.2}$$

with mixed parameters consistently chosen according to the following Lorentz-Berthelot combination rules

$$\sigma_{ij}=\frac{1}{2}(\sigma_{ii}+\sigma_{jj}) \quad \text{and} \quad \varepsilon_{ij}=\left(\varepsilon_{ii}\cdot\varepsilon_{jj}\right)^{1/2}; \tag{2.3}$$

(ii) a Coulomb term

$$U_C(r_{ij}) = \frac{1}{4\pi\varepsilon_0}\frac{q_i q_j}{r_{ij}}, \tag{2.4}$$

being ε_0 the permittivity in a vacuum, and q_i, q_j the partial charges of atoms i and j, respectively. Non-zero partial charges are assigned only to atoms at the surface of the pore and belonging to a silanol group, whereas all other atoms (bulk of silica) are considered neutral (i.e. zero partial charge, q_i=0). More specifically, partial charges in a silanol group are assigned following the criterion of the overall neutral charge for the entire system, with nonbonded parameters for silica reported in Reference [148].

Similarly to silica, partial charges are assigned only to atoms at the magnetite surface and belonging to the Fe-O-H groups, whereas zero partial charges (i.e. q_i=0) are imposed at all other bulk atoms. Moreover, partial charges are assigned within the Fe-O-H groups in order to ensure neutrality of the whole system. Both the adopted parameterization for Lennard-Jones potentials and the partial charges are reported in References [149] and [150]. For the sake of completeness, Lennard-Jones parameters and partial charge values have been further artificially changed in some MD setups, in order to perform sensitivity analyses of force field parameters on D.

Nonbonded interactions between CNTs and water molecules are modeled by Lennard-Jones potential (Equations 2.2 and 2.3), where carbon atoms are characterized by $\sigma_{CC} = 0.36$ nm and $\varepsilon_{CC} = 0.29$ kJ mol^{-1} [145–147]. All nanotubes' carbon atoms are considered as neutral, because of the strong hydrophobicity of pristine CNTs.

Finally, Lennard-Jones potentials are treated with a twin-range cut-off and 1.5 nm cut-off distance, whereas a Particle-Mesh Ewald (PME) [16] with 1.5 nm real-space cutoff, a 0.12 nm reciprocal space gridding, and splines of order 4 with 10^{-5} tolerance is used for electrostatic interactions.

2.2.3. Simulation protocol

Simulations are carried out with a leap-frog algorithm (time step: $\Delta t = 0.5$ fs), and periodic boundary conditions are applied along the three Cartesian coordinates. Upon energy minimization of nanoparticle, nanopore or

nanotube setups, the two sub-systems (solid crystals and water) are initialized at 300 K (Maxwellian distribution of velocities), and fully coupled to a Nosé-Hoover thermostat [151, 152] (at 300 K and time constant $\tau =$ 0.2 ps) for 50 ps, until the energies of the system relax to a steady state. During the latter preliminary calculation, one thermostat for each subsystem is adopted. Afterwards, Nosé-Hoover thermostats (at 300 K) are maintained attached to solid crystals only, whereas the simulation is continued up to 2 ns. In case of proteins, the MD protocol is slightly changed to improve convergence. Energy minimization for proteins is performed before and after solvation and ions are added (when needed) for achieving the neutrality of the system, which is then equilibrated in two steps: 100 ps in canonical ensemble (NVT) at 300 K (initialization with Maxwellian distribution of velocities, Berendsen thermostats [153] separately attached to proteins and water, $\tau = 0.1$ ps); 100 ps in NPT ensemble at 300 K and 1 bar (Berendsen thermostats separately attached to proteins and water, $\tau = 0.1$ ps; Parrinello-Rahman pressostat [154] applied to the whole system, $\tau = 2$ ps). During the equilibration, all bonds in the proteins are kept rigid using the LINCS algorithm [155]. Finally, a Nosé-Hoover thermostat (300 K, $\tau = 0.2$ ps) is attached to protein's atoms, and the simulation is continued for 1 ns.

The SPC/E model [156] is used for water molecules, which is known to accurately predict some of the properties of water relevant for this study at room temperature [157]. However, it is also worth noticing that the SPC/E model does not accurately predict some other properties of water. For instance, shear viscosity or thermal conductivity are found to be off by more than 50% at room temperature [158].

The MD simulations are performed with the software package GROMACS [159]. Rendering is performed with UCSF Chimera [160].

2.3. Molecular Dynamics results

In this Section, the MD setups analyzed for investigating the effect of geometrical, chemical and physical parameters on water self-diffusivity under nanoconfined conditions are presented. First, MD simulations are checked for convergence; second, results of both water density and D are reported.

2.3.1. Simulated cases

In order to investigate the influence of geometry and material properties, the self-diffusion coefficient of nanoconfined water molecules is computed for 58 different cases. First, for assessing the effect of particle geometry on D, these cases are different in terms of NP diameter, being 1.3, 2.0 or 5.2 nm; nanopore diameter, with values 2.0, 4.1, 8.1 and 11.0 nm; number of NPs adsorbed on the nanopore wall, varying from 0 to 66 NPs per pore; CNT armchair chirality, namely (5,5), (10,10), (20,20) and (30,30); and type of proteins, including molecules with a spherical (e.g. Ubiquitin) and elongated (e.g. Ca^{2+}-ATPase) shapes; of small (e.g. 562 atoms of B1-immunoglobulin binding domain) and large (e.g. 9667 atoms of Ca^{2+}-ATPase) sizes; and exhibiting a catalytic (e.g. Glucokinase), hormonal (e.g. Leptin), and transport (e.g. Myoglobin) function. Second, for assessing the effect of material properties on D, the strength of the Lennard-Jones potential of magnetite NPs is varied from 2.49 to 24.94 kJ mol^{-1}, and the partial electrostatic charges of atoms are set to either the nominal value or zero, for NPs and nanopores. Finally, various hydration levels are considered providing an overall water density ranging from 715 to 941 kg m^{-3}. Note that for these density values, there is no heterogeneous wetting and consequently no anomalous behavior related to low water filling regimes [42, 92]. All computed values of the self-diffusion coefficient D are reported in the Appendix B.

Finally, the influence of temperature on D is explored, considering Case 7 as a reference and changing the temperature of the system to 350 K and 280 K, the measured D are $3.37 \pm 0.14 \times 10^{-9}$ $m^2 s^{-1}$ and $0.86 \pm 0.03 \times 10^{-9}$ $m^2 s^{-1}$, which implies a linear trend between D and temperature, in accordance with the Einstein relation. However, the anomalous dynamics of nanoconfined water at different temperatures [42, 161] and the supercooled regime at low temperatures [32, 37] are beyond the aims of this thesis and will require further investigations.

2.3.2. Convergence of simulations

First, the analyzed systems are equilibrated in order to measure the self-diffusion coefficient D of water molecules at equilibrium conditions. In Figures 2.9 and 2.10, the steady state energies of configurations made out of solvated nanopores and solvated nanopores filled by NPs are shown, respectively.

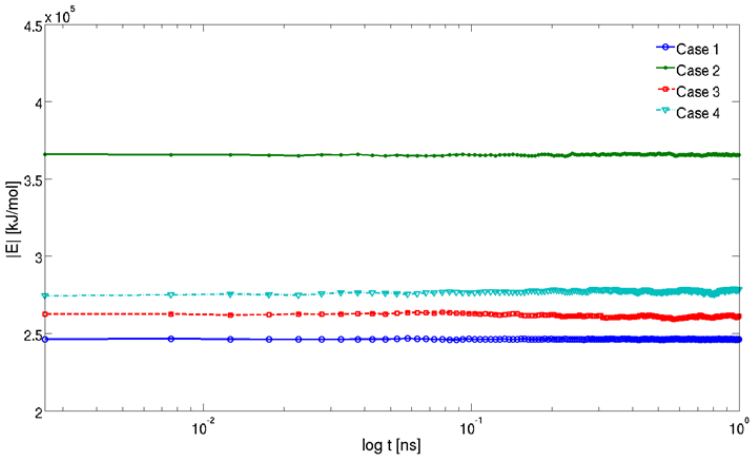

Figure 2.9.: Total energy conservation in the systems where silica nanopores are simulated (Cases 1−4 in Table B.1). D is obtained from the MSD calculated between 600 and 1000 ps.

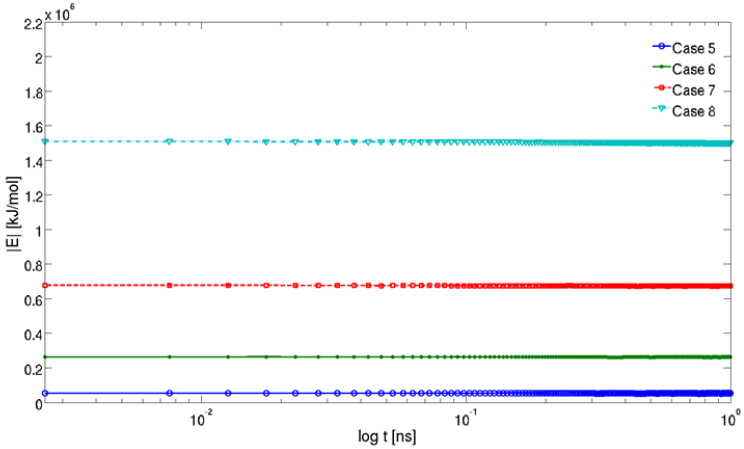

Figure 2.10.: Total energy conservation in the systems where magnetite NPs within silica nanopores are simulated (Cases 5−8 in Table B.2). D is obtained from the MSD calculated between 600 and 1000 ps.

Hence, D is determined following the classical relationship of Einstein and computing the mean square displacement (MSD) as

$$MSD = \lim_{t\to\infty} \left\langle \left\| \overrightarrow{r_i}(t) - \overrightarrow{r_i}(0) \right\|^2 \right\rangle_{i\in water} = 6Dt, \tag{2.5}$$

where the position vector $\overrightarrow{r_i}$ refers to the center of mass of the water molecule i at the generic time t, and 0 refers to the initial configuration of the system (in Figures 2.11 and 2.12 a few cases are shown) [16, 162]. Alternative approaches for computing the water diffusivity could be considered as well (e.g. those based on the first-passage concept) [163, 164]. Note that the MSD trend is linear after few picoseconds ($MSD \propto t^{\alpha}$, with $\alpha = 1$), which denotes classical diffusion by Brownian motion. Figure 2.14 depicts a double logarithmic plot of MSD versus time, where three different segments can be clearer distinguished, indicating three different diffusive regimes: (i) a ballistic region ($\alpha \cong 2$) [165], within a sub-picosecond domain; (ii) a cage breaking sub-diffusion regime ($\alpha < 1$) [166], within 1–50 ps according to the different configurations; (iii) the Brownian diffusion regime ($\alpha = 1$), where D of water is actually evaluated. Note that, in cases where water molecules are highly confined (e.g. Case 1 in Table B.1), the sub-diffusion regime can last tens of picoseconds, because the proximity of most of the water to a surface significantly affects the cage-breaking needed by the diffusing molecules for escaping their own hydration shell [166, 167].

Finally, the convergence of D in 1 ns runs is verified by evaluating it every 200 ps and by verifying that D tends to an asymptotic value, as shown for example in Figure 2.14. For the sake of completeness, a few setups are extended up to 2 ns, in order to further assess the stability of D in longer runs. The extended simulations confirm that D converges to a steady state value after approximately 0.6 ns, then it fluctuates (less than $\pm 10\%$) around the equilibrium value.

After a few hundreds of picoseconds, the stability of the simulated protein structures is also assured by the convergence of: (i) systems' energies; (ii) root mean square deviation of the structures with respect to the crystallographic ones (averagely below 0.3 nm, e.g. Figure 2.15a); (iii) radius of gyration of the protein (e.g. Figure 2.15b).

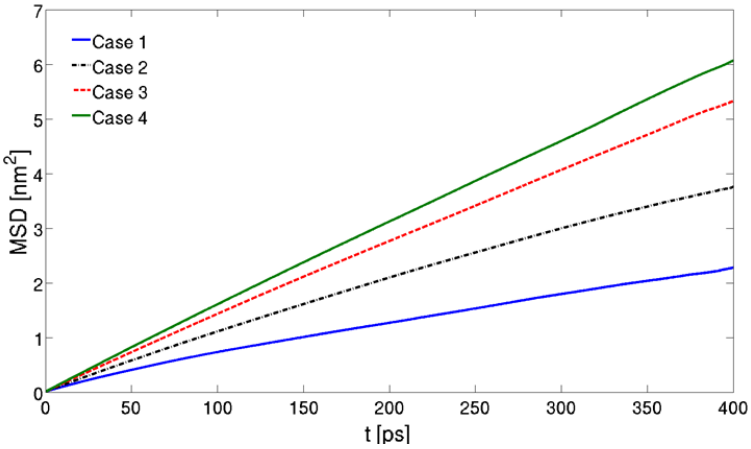

Figure 2.11.: MSD of water in nanopore setups. MSD is evaluated on equilibrated systems between 600 and 1000 ps. Silica nanopores are simulated (Cases 1−4 in Table B.1).

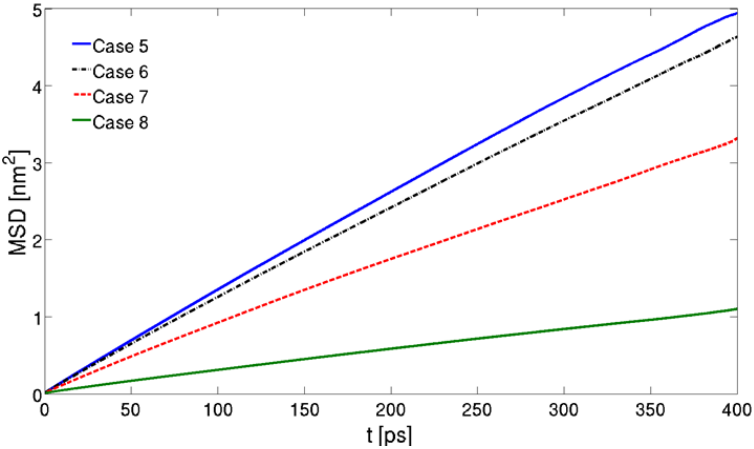

Figure 2.12.: MSD of water in nanopore filled by NPs setups. MSD is evaluated on equilibrated systems between 600 and 1000 ps. Magnetite NPs within silica nanopores are simulated (Cases 5−8 in Table B.2).

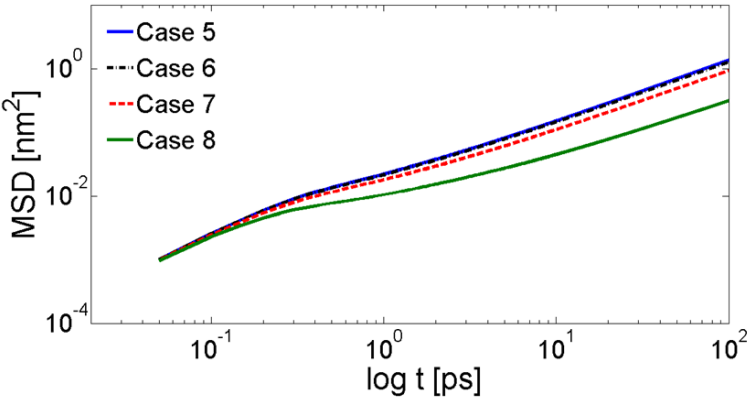

Figure 2.13.: Double logarithmic plot of MSD versus time, evaluated on equilibrated systems between 600 and 1000 ps. Magnetite NPs within silica nanopores are simulated (Cases 5−8 in Table B.2).

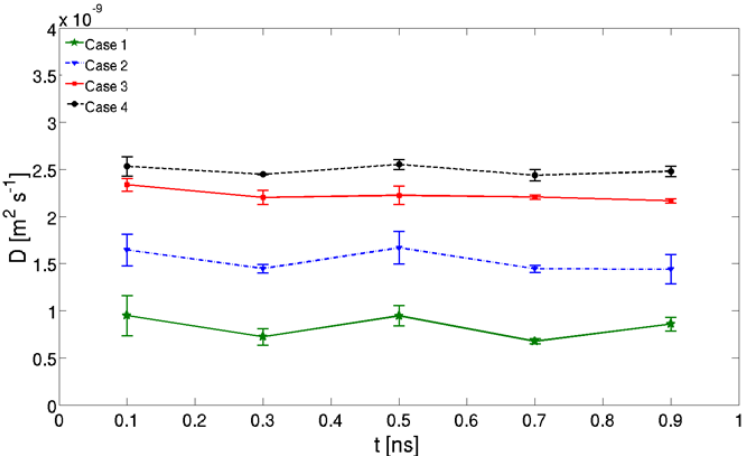

Figure 2.14.: D versus time in equilibrated nanopore setups. Silica nanopores are simulated (Cases 1−4 in Table B.1). Error bars are obtained by fitting MSD in different time intervals.

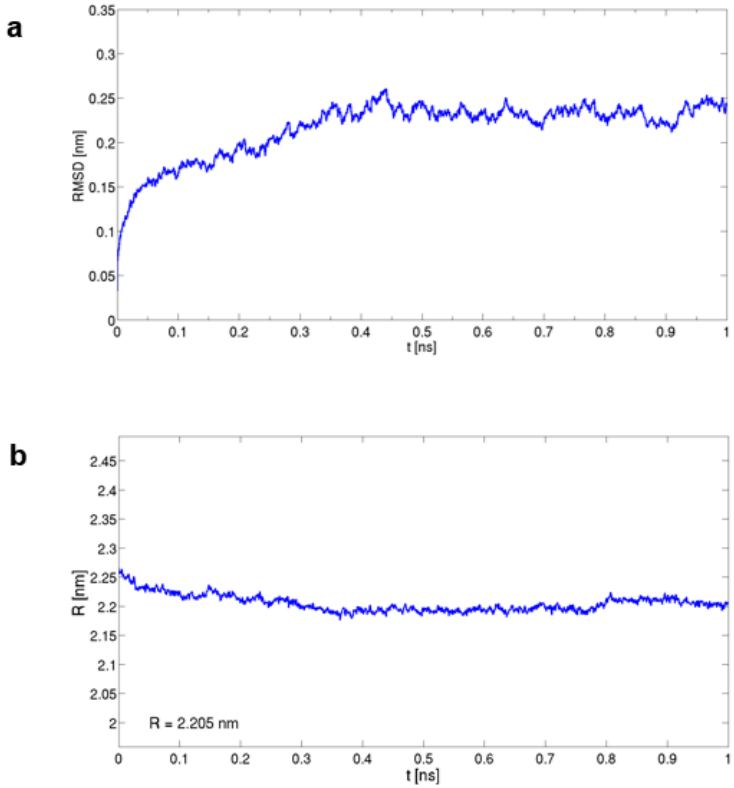

Figure 2.15.: Structure stability of Glucokinase in 1 ns MD simulation. (a) Root mean square deviation. (b) Radius of gyration.

2.3.3. Density of water at the interface

Water molecules in a close proximity of solid surfaces are subject to van der Waals and Coulomb interactions, which interfere with their dynamics. This induces a layering of water molecules near the surface. Among these layers, only the first and partially the second layer of water (i.e. within 0.3–1.0 nm from the solid surface [168]) show appreciable different physical properties as compared to bulk water [88, 169].

In Figure 2.16, the density (ρ) of water within a silica nanopore, around a magnetite NP and in a silica nanopore with magnetite NPs are shown. In

all simulated cases, the density profile is clearly flat over 0.5–1.0 nm from the solid surface, according to the different geometries and force fields used. Layering effects of water can be noticed at the solid interface, where water is organized in a mono, double or more layer structure.

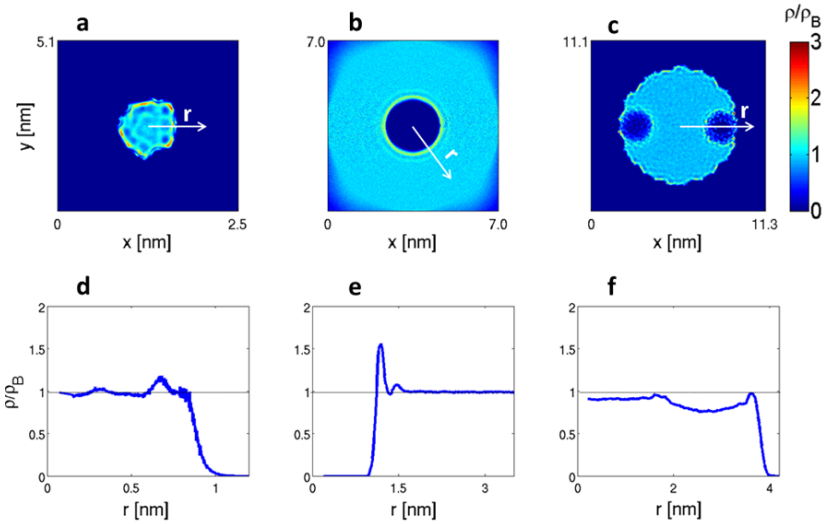

Figure 2.16.: Water density (ρ) within nanopores or around NPs. All density values are normalized by the bulk density $\rho_B = 1000$ kg m^{-3} at 300 K. (a) 2D distribution of ρ/ρ_B within a silica nanopore ($\Phi = 2.0$ nm), which is calculated by averaging ρ along the nanopore axis. (b) 2D distribution of ρ/ρ_B around a magnetite NP ($\phi = 2.0$ nm) within a cubic water box ($L = 7.0$ nm), which is calculated by averaging ρ along the radius of NP. (c) 2D distribution of ρ/ρ_B within a silica nanopore ($\Phi = 8.1$ nm) filled by 4 magnetite NPs ($\phi = 2.0$ nm), which is again calculated by averaging ρ along the nanopore axis. Only 2 out of 4 NPs are visible, because they are placed on the same x, y coordinates along the pore axis. (d) Radial ρ/ρ_B within a silica nanopore ($\Phi = 2.0$ nm), where $r = 0$ nm lies on nanopore axis. (e) Radial ρ/ρ_B around a magnetite NP ($\phi = 2.0$ nm), where $r = 0$ nm lies on NP barycenter. (f) Radial ρ/ρ_B within a silica nanopore ($\Phi = 8.1$ nm) filled by 8 magnetite NPs ($\phi = 2.0$ nm), where $r = 0$ nm lies on nanopore axis.

The first layer of water around the surface of a silica nanopore (Φ = 2 nm) shows a peak of 1.2 ρ/ρ_B (ρ_B = 1000 kg m^{-3} is the bulk density at 300 K). A second layer is barely observable at r = 0.4 nm from the center of the pore. Moreover, local peaks of 2.5-3.0 ρ/ρ_B can be noticed in the narrower cavities at the pore surface (Figure 2.16a,d). In Figure 2.17 the water densities within nanopores with different diameters are compared. It is possible to notice that an higher diameter implies a greater region of bulk water, because the interface region (i.e. the first layers of water) is still relegated to the first 0.5–1.0 nm from the solid surface. Moreover, the peak intensity of the first layer of water is almost the same in all cases, i.e. 1.2 ρ/ρ_B.

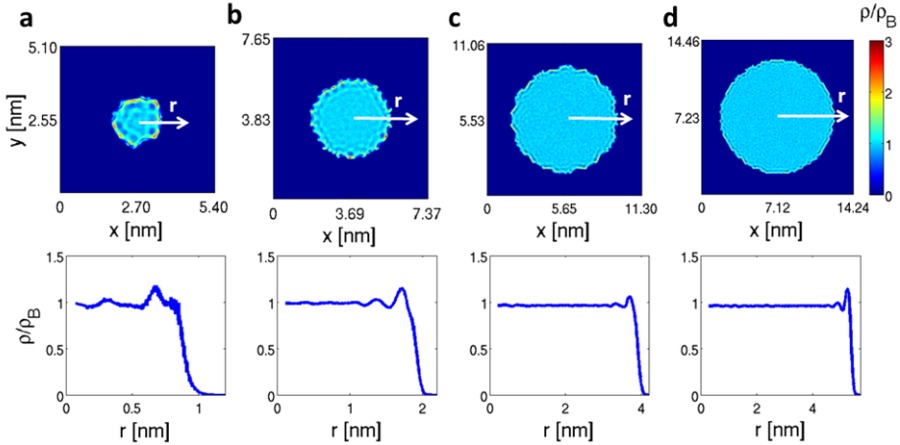

Figure 2.17.: Water density (ρ) within nanopores with different diameters. (a) Φ = 2.0 nm; (b) Φ = 4.1 nm; (c) Φ = 8.1 nm; (d) Φ = 11.0 nm. Top: the 2D distribution of ρ/ρ_B within silica nanopores is depicted, which is calculated by averaging ρ along the nanopore axis. Bottom: the radial ρ/ρ_B within silica nanopores is shown, where r = 0 nm lies on nanopore axis.

For the magnetite NP (ϕ = 2.0 nm), the first layer of water shows a clear peak of 1.5 ρ/ρ_B, and a second layer of water is also visible with a peak of 1.1 ρ/ρ_B (Figure 2.16b,e). The higher peak in the density profile for magnetite is determined by the selection of stronger Lennard-Jones and Coulomb interactions [27].

The density distribution of water within a system composed by a silica nanopore (Φ = 8.1 nm) filled by 4 magnetite NPs (ϕ = 2.0 nm) is then considered. In Figure 2.16c, local peaks of 2.5-3.0 ρ/ρ_B can be noticed around the NPs and in the narrower cavities of the nanopore, with a synergistic effect in the interstices between NPs and nanopore surface; whereas in Figure 2.16f the radial distribution of ρ/ρ_B shows an expected drop in water density where the NPs are located. However, ρ/ρ_B peaks are still noticeable around NPs and nanopore surfaces, even though radially averaged with the rest of bulk water within the nanopore.

Finally, the density distribution of water around (and within) a (20,20) CNT is considered. In Figure 2.18, local peaks of 2.3 ρ/ρ_B can be noticed in the proximity of CNT surface. Notice that the apparently asymmetric distribution of water densification around the CNT is given by the slight tumbling of the geometry around the y axis during the simulation.

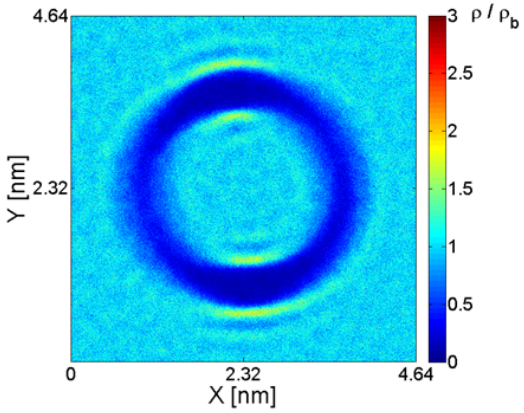

Figure 2.18.: Water density (ρ) within CNT. Density values are normalized by the bulk density ρ_B = 1000 kg m^{-3} at 300 K. The 2D distribution of ρ/ρ_B within and around a (20,20) CNT 10 nm long is depicted, which is calculated by averaging ρ along the CNT axis (i.e. z axis).

Note that the hydrophilic liquid-solid interaction within the first layers of adsorbed water induces a strong distortion of the hydrogen bond network, which in turn significantly affects the dynamics of confined water [170, 171].

Of course, the level of hydration determines the effective pressure, namely

the sum of the bulk pressure and the spreading pressure [25], inside the low mobility region due to nanoconfinement and consequently to the thermodynamic state of water in the low mobility region. Eventually, the effective pressure could determine a switch from a low-density liquid to a high-density liquid [17]. The observations here refer to the mobility of nanoconfined water, which are not greatly affected by the actual local density.

2.3.4. Self-diffusivity of nanoconfined water

In general, results reported in Appendix B show that the coefficient D decreases compared to the bulk value, 2.60×10^{-9} m^2s^{-1} at 300 K [157], as the ratio between the total area of the solid-liquid interface and the total volume occupied by the water (V_w) increases. More specifically, for a silica nanopore, D is reduced from $2.50\pm0.09\times10^{-9}$ m^2s^{-1} to $0.82\pm0.22\times10^{-9}$ m^2s^{-1} as the pore diameter decreases from 11.0 to 2.0 nm. Moreover, D is inversely proportional to the NP concentration and diameter. For a 5.2 nm silica NP, D decreases from the almost unconfined value to $2.12 \pm 0.04 \times 10^{-9}$ m^2s^{-1} following a 36% increase in NP concentration. Indeed, the increase in NP concentration is associated with a decrease in separation distance between adjacent NPs and, consequently, a decrease in the volume available to water molecules. Consistently, D reduces as the concentration of magnetite NP increases within a nanopore: D is $2.20 \pm 0.10 \times 10^{-9}$ m^2s^{-1} in a 8.1 nm silica nanopore; however, if 2 magnetite NPs, of 2.0 nm in diameter, are adsorbed on the nanopore surface, D decreases to $2.07 \pm 0.14 \times 10^{-9}$ m^2s^{-1} and it drops to $0.44 \pm 0.05 \times 10^{-9}$ m^2s^{-1} ($\sim$80% decrease), if 16 magnetite NPs, of 2.0 nm in diameter, are added in the nanopore. In addition, for 16 magnetite NPs adsorbed on the wall of a 8.1 nm nanopore, D is $1.46 \pm 0.09 \times 10^{-9}$ m^2s^{-1} for 1.3 nm NPs and becomes $0.44\pm0.05\times10^{-9}$ m^2s^{-1} ($\sim$70% decrease), for 2.0 nm NPs. A similar trend is observed for the carbon nanotubes and proteins, by reducing the size of the water box. More specifically, around the (5,5) chirality CNT with a length of 5 nm, the water diffusivity D decreases from the bulk value (box of 316 nm^3) to $1.22\pm0.12\times10^{-9}$ m^2s^{-1} (box of 21 nm^3). Similarly, around the B1-immunoglobulin binding domain, the diffusivity D decreases from $2.41\pm0.04\times10^{-9}$ m^2s^{-1} (box of 348 nm^3) to $0.87\pm0.10\times10^{-9}$ m^2s^{-1} (box of 23 nm^3). As expected, the above data qualitatively demonstrate that the self-diffusion coefficient D of water is strongly correlated to the ratio between the interface surface and the total water volume: the larger this

ratio the smaller the water mobility. However, the possible contribution of other parameters should also be assessed.

To this end, sensitivity analyses are performed to elucidate the effect of the Lennard-Jones potential strength ε and Coulomb interactions on D. Larger values of the parameter ε are associated with lower mobility of the water molecules. As an example, let us consider the case of 8 magnetite NPs (2.0 nm diameter) adsorbed on the walls of a 8.1 nm diameter silica nanopore. A one order of magnitude decrease of ε of magnetite atoms only carries a 10 percent increase of D: for $\varepsilon = 24.94$ kJ mol^{-1} D is equal to $1.33 \pm 0.13 \times 10^{-9}$ m^{2}s^{-1}, whereas D increases to $1.47 \pm 0.11 \times 10^{-9}$ m^{2}s^{-1} for $\varepsilon = 2.49$ kJ mol^{-1}. Moreover, D increases as the surface electrostatic charges decrease. For neutral magnetite NPs, D grows to $1.64 \pm 0.04 \times 10^{-9}$ m^{2}s^{-1} and, if both the NPs and nanopore wall are electrically neutral, D takes the value of $1.69 \pm 0.20 \times 10^{-9}$ m^{2}s^{-1} ($\sim$30% increase as compared to the example above). Although the water molecule confinement is affected by the strength of the interaction potentials (van der Waals and Coulomb), geometrical parameters show a greater influence on the coefficient D. The reason is that all considered surfaces have effective wall potentials, which are strong enough to induce a significant reduction of the water mobility in a region close to the wall. On the other hand, as clarified below, the volume of the low mobility region only slightly depends on the wall potential strength, namely the minimum of the potential well generated by the wall.

Finally, the self-diffusion coefficient D does not change significantly with the level of hydration in the considered range, in accordance with previous studies [92]. Considering again the representative case of 8 magnetite NPs, of 2.0 nm in diameter, adsorbed on the wall of a 8.1 nm silica nanopore, D ranges from $1.30 \pm 0.11 \times 10^{-9}$ to $1.40 \pm 0.07 \times 10^{-9}$ m^{2}s^{-1} ($< 10\%$ variation), as the water density increases from 700 to 930 kg m^{-3}.

2.4. Scaling self-diffusivity of nanoconfined water

In this Section, self-diffusion coefficients of nanoconfined water obtained by MD simulations and literature review are scaled by defining a characteristic length of nanoconfinement δ of solid interfaces, which depends on the solid-liquid nonbonded interaction energies, and by introducing a novel

dimensionless parameter θ, which allows to compare the broad variety of nanoconfined configurations.

2.4.1. Characteristic length of nanoconfinement

In the bulk fluid, the water molecules fluctuate with a kinetic energy proportional to $k_B T$, where k_B is the Boltzmann constant (1.38×10^{-23} J K^{-1}) and T is the temperature. As opposed to molecules in the bulk, those in a close proximity of solid surfaces are subjected to additional van der Waals (U_{vdw}) and Coulomb (U_c) interactions interfering with their state of agitation. This induces a layering of water molecules with reduced mobility near the solid surface (see Figures 2.16), as already pointed out in other works [32, 172]. A characteristic length δ can be introduced to quantify the thickness of such confined water layer.

Referring to the popular notion of Solvent Accessible Surfaces (SAS) [173–175], the quantities S_{tot} and S_{loc} can be introduced as the total and specific (per-atom) SAS areas, respectively. For an arbitrary atom i of the solid structure, a number N_n of nearest neighbors (including the atom i itself) can be identified within a fixed cut-off radius (Figure 2.19a,c). The corresponding effective potential energy U_{eff} on the water molecules, due to both the van der Waals (U_{vdw}) and Coulomb (U_c) interactions, can be computed as:

$$U_{eff}(n) = U_{vdw}(n) + \langle U_c \rangle (n), \tag{2.6}$$

along the n-direction, orthogonally to the SAS and passing through the center of the atom i (Figure 2.19c). For the 12-6 Lennard-Jones potential, it follows that

$$U_{vdw}(n) = \sum_{k=1}^{N_n} 4\varepsilon_k \left[\left(\frac{\sigma_k}{r_k} \right)^{12} - \left(\frac{\sigma_k}{r_k} \right)^{6} \right], \tag{2.7}$$

with ε_k, σ_k and r_k denoting the depth of the potential well, the distance at with such potential becomes zero, and the Euclidean distance between the generic line point with coordinate n and the center of $k-th$ nearest neighbor, respectively. Note that, when defining the van der Waals potential $U_{vdw}(n)$ in Equation 2.7, the parameters ε_k and σ_k already incorporate a combination rule for the Lennard-Jones parameters between the atom i and oxygen atoms of water (e.g. the Lorentz-Berthelot rule). For the

Coulomb interactions, the average potential energy at a fixed temperature T between the N_n atoms and the water dipoles is

$$\langle U_c \rangle (n) = -E\mu_w \Gamma \left(\frac{E\mu_w}{k_B T} \right), \tag{2.8}$$

where E, μ_w, k_B and Γ denote the electrical field strength, water dipole moment (7.50×10^{-30} C m for SPC/E model), the Boltzmann constant and the Langevin function

$$\Gamma (x) = \coth (x) - 1/x. \tag{2.9}$$

In Equation 2.8, the effective strength of the electrical field $E(n) = \|\mathbf{E}(n)\|$ may be expressed by the following explicit form:

$$E (n) = \frac{1}{4\pi\varepsilon_0\varepsilon_r} \left\| \sum_{k=1}^{N_n} q_k \nabla \left(\frac{1}{r_k (n)} \right) \right\|, \tag{2.10}$$

$$r_k (n) = \sqrt{[x (n) - x_k]^2 + [y (n) - y_k]^2 + [z (n) - z_k]^2}, \tag{2.11}$$

being q_k the electric charge of the $k - th$ neighbor, while (x, y, z) and (x_k, y_k, z_k) representing the Cartesian coordinates of the generic point on l (corresponding to the local coordinate n) and the Cartesian coordinates of neighbor k, respectively. In our approach, the relative permittivity ε_r is an input parameter to be provided to the Matlab® routine WANA for the computation of δ (see Appendix C). In particular, here ε_r is included as a function of the distance from the particle ($\varepsilon_r(n)$), following the suggestion in Reference [176].

The expression of $\langle U_c \rangle (n)$ is a classical result of electrostatics and can be justified as follows. Let $\mathbf{E}$ be the electric field acting on a dipole μ. The instantaneous energy can be expressed as $U_c (\varphi) = -\mu \cdot \mathbf{E} = -\mu E \cos\varphi$, with E and μ being the field and dipole strength, respectively, while φ is the angle between the direction of the dipole and the field. The minimum and maximum values of energy are attained for $\varphi = 0$ and π, respectively. However, in the presence of thermal agitation, the direction of μ (hence φ) continuously changes in time. For classical systems, a number of independent dipoles are distributed according to their energy level $U_c : U_{c,min} < U_c < U_{c,max}$. In particular, at thermodynamic equilibrium, the Boltzmann distribution predicts that the number $N(U_c)$ of dipoles with energy U_c is:

$$N (U_c) = C \exp \left(-\frac{U_c}{k_B T} \right), \tag{2.12}$$

being C a constant to be determined. Note that, in three dimensions, all dipoles lying on a cone with angle 2φ around the electrical field direction have the same energy. Moreover, at every φ, the total number of such dipoles is $N\left(U_c\left(\varphi\right)\right)d\Omega$, being Ω the incremental solid angle. The above dipoles at φ give the component sum $d\mu$ in the field direction: $d\mu = Nd\Omega\mu\cos\varphi$. Hence, according to the Boltzmann distribution, the average dipole moment takes the more explicit form:

$$\langle\mu\rangle = \mu\frac{\int_0^\pi \exp\left(\frac{\mu E\cos\varphi}{k_B T}\right)\sin\varphi\cos\varphi d\varphi}{\int_0^\pi \exp\left(\frac{\mu E\cos\varphi}{k_B T}\right)\sin\varphi d\varphi}. \tag{2.13}$$

Upon substituting $\beta = \mu E/k_B T$ and $\zeta = \cos\varphi$, the above integral becomes $\langle\mu\rangle = \mu\Gamma\left(\beta\right)$.

Knowing the effective potential $U_{eff}\left(n\right)$ for the atom i, a corresponding characteristic length δ_i can be estimated within which the water molecules have reduced mobility. This length δ_i is given by $\delta_i = n_{i,2} - n_{i,1}$, where $n_{i,2}$ and $n_{i,1}$ (Figure 2.19b) are the two zeros of the equation

$$U_{eff}\left(n\right) + \alpha k_B T = 0, \tag{2.14}$$

where we expect $\alpha \approx 1/4$. In fact, provided that $k_B T/2$ is the kinetic energy attributed to each degree of freedom of the water molecules, for planar surfaces $\alpha = 1/4$ because molecule are allowed to escape the potential well only along half of the direction orthogonal to the surface. Obviously, when the horizontal line $U + \alpha k_B T = 0$ does not intersect the function in Equation 2.6, $\delta_i = 0$.

Therefore, based on the definition of δ_i, all the water molecules located within such a distance are significantly affected by the van der Walls and Coulomb interactions, whereas all the water molecules beyond the characteristic length δ_i can escape the potential well generated by the solid wall. In general, the quantity δ_i varies at each atom i (see Figure 2.19a). Moreover, (meaningless) non-zero values for δ_i can be found for bulk atoms. By proper averaging over the surface, the mean characteristic length δ of the overall solid surface (Figure 2.19d) can be derived as

$$\delta = \frac{\sum_{i=1}^{N}\delta_i S_{loc,i}}{S_{tot}}, \tag{2.15}$$

being $S_{loc,i}$ and N the specific (per-atom) SAS for the atom i and the total number of atoms, respectively. Note that the above formulation is general

and applies to hydrophilic and hydrophobic surfaces, regardless of their electrostatic surface charge. Also, both S_{tot} and $S_{loc,i}$ are readily computed by GROMACS, once the geometry of the system is known (e.g. in the form of a **.pdb* file). It is also worth emphasizing that δ is a characteristic length of the whole system of interest and can be straightforwardly computed based on the geometry, Lennard-Jones force field parameters and partial charges. The script for computing δ is based on Matlab® and it is provided in Appendix C (WANA software).

In Figure 2.20, the water density profiles within a silica nanopore and around a single magnetite NP are shown, where peaks denote the typical water layers nearby a solid wall at the nanoscale [32, 88]. The abscissa r_n represents the radial distance from either the pore wall or the NP surface. It is worth noting that despite the great difference in the potential strength between silica and magnetite ($\min U_{eff,2}/\min U_{eff,1} \approx 2.7$), the corresponding difference in terms of characteristic lengths is much more moderate ($\delta_2/\delta_1 \approx 1.5$). From the density profiles, magnetite clearly induces a stronger perturbation in the nearby water molecules distribution. However, except for a first thin water layer strongly adsorbed to the NP surface (and accounted by $\delta_2 > \delta_1$), the amplitude of these perturbations rapidly decays further away and become comparable in the remaining confined volume for both cases. Similarly, even though there is a significant difference in the potential minimum between Green Fluorescence Protein and (5,5) CNT ($\min U_{eff,2}/\min U_{eff,1} \approx 1.5$), the difference between the two characteristic lengths is negligible. The above observations suggest that geometrical parameters could more significantly affect D as compared to energetic parameters.

2.4.2. Scaling law

Finding a proper parameter θ (or equivalently δ) for scaling the self-diffusivity of nanoconfined water in such a large variety of configuration is not trivial. A few unsuccessful attempts to find a general scaling parameter for water self-diffusion coefficient have been tried, and they are reported in Appendix A.

Since water mobility is impaired mostly in a thin layer next to the liquid-solid interface with thickness δ, it is reasonable to assume that the observed variation in the self-diffusion coefficient D is mainly associated with the altered mobility of the water molecules within such a layer and the corresponding volume (volume of influence – Figure 2.20). Also, it has been

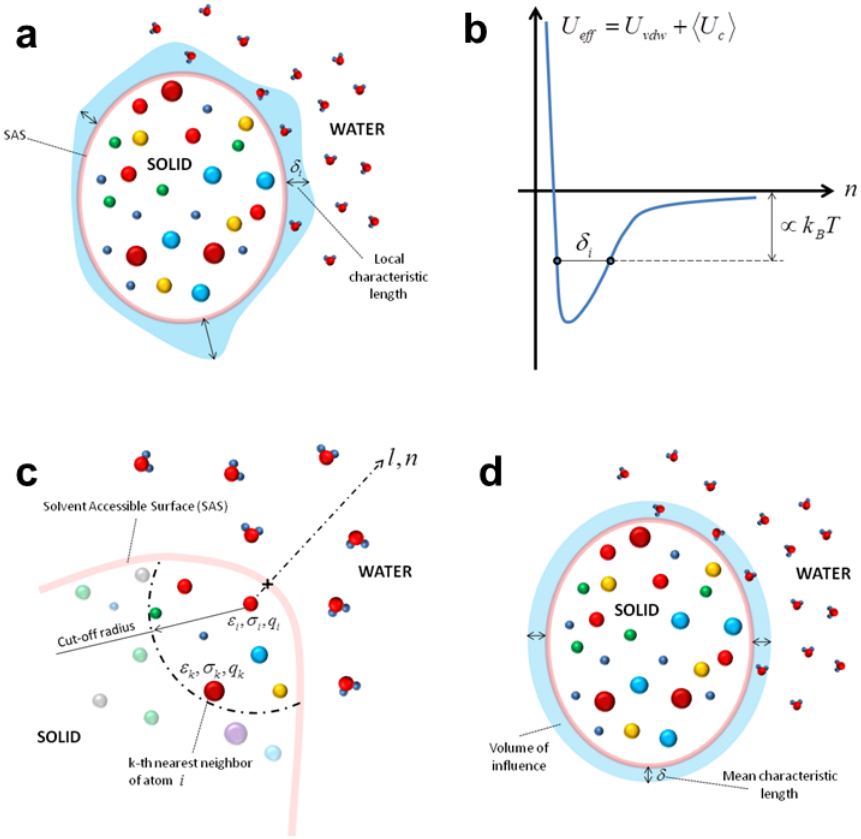

Figure 2.19.: The characteristic length of nanoconfinement δ. (a) A local characteristic length δ_i can be defined at any atom i (with non vanishing Solvent Accessible Surface - SAS). (b) The thermal energy level provides a criterion to (locally) define the characteristic length δ_i, which typically varies along the whole SAS. (c) The contribution to the total potential energy of neighbors along a direction orthogonal to the SAS (line l with local coordinate n) is computed. (d) A characteristic length of nanoconfinement δ for the whole structure can be defined by a weighted average of all δ_i. Figure adapted from Reference [27].

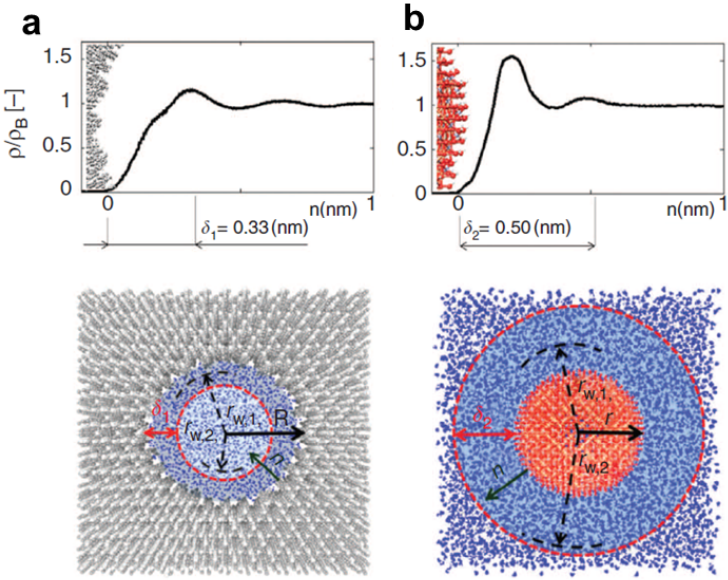

Figure 2.20.: Length of nanoconfinement δ of a nanopore and a nanoparticle. (a) The length of nanoconfinement is reported for a silica nanopore ($\delta_1 \approx 0.33$ nm) and (b) for a magnetite nanoparticle ($\delta_2 \approx 0.50$ nm). For silica, only the first water layer (with distance $r_{w,1}$ from the pore axis) is located within the volume of influence. For magnetite, both the first and the second water layers (with distances $r_{w,1}$ and $r_{w,2}$ from the particle center respectively) are found within the volume of influence. Figure adapted from Reference [27].

already observed that the self-diffusion coefficient D reduces as the ratio between the total interfacial area and the total volume occupied by water increases. Based on such an evidence, a scaling parameter θ can be introduced as the ratio between the total water volume of influence (V_{in}) and the total volume accessible to the water molecules (V_w), thus

$$\theta = \frac{V_{in}}{V_w} \approx \frac{\sum_p S_{tot}^{(p)} \delta^{(p)}}{V_w}. \tag{2.16}$$

This dimensionless parameter θ varies from 0 (bulk water case) to 1 (totally confined water). The volume of influence (V_{in}) is the volume of water that feels the van der Walls and Coulomb interactions and is therefore influenced by the presence of solid walls. This volume is readily given by

$$V_{in} \approx \sum_{p} S_{tot}^{(p)} \delta^{(p)}, \tag{2.17}$$

where $S_{tot}^{(p)}$ and $\delta^{(p)}$ represent the total SAS and characteristic length of the $p-th$ particle, respectively. In Equation 2.17, the particle curvature is neglected, thus this is accurate in the limit $\delta^{(p)} \ll r^{(p)}$, being $r^{(p)}$ a representative radius of curvature of the $p-th$ particle. However, if the latter approximation is not properly fulfilled, a more accurate estimate of the numerator at the right-hand side of Equation 2.17 can be easily adopted.

Clearly, in cases of strong confinement (and high values of δ) with the presence of several particles (e.g., the reported studies where a number of spherical nanoparticles are loaded within cylindrical nanopores) a partial overlap of the volumes of influence progressively becomes more probable. However, we notice that volumes of influence due to different particles are not additive. As a result, the quantity θ computed by Equation 2.16 is only apparent, with the effective fraction of the volume of influence being smaller than θ. The above issue is usually encountered in the framework of Continuum Percolation Theory (CPT). Under the assumption of randomly placed volumes, a classical result of CPT suggests that, in order to properly recover the effective fraction, the apparent volume fraction should be corrected as [177, 178]

$$\theta^{'} = 1 - \exp\left(-\theta\right). \tag{2.18}$$

Hence, the above correction applies in the presence of overlap of the volumes of influence (e.g. several particles within the computational box).

As seen in Equation 2.16, the evaluation of θ is also influenced by the estimation of the overall water volume in the considered nanoconfined configuration (V_w). For fully hydrated simple geometries, V_w can be computed by considering the nominal size of a particle/pore. However, in general, the volume V_w can be defined as:

$$V_w = N_{sol}/\rho_n, \tag{2.19}$$

where N_{sol} and ρ_n are the number of water molecules within the computational periodic box and the average water number density, respectively.

As a consequence, the volume occupied by a solvated particle p is $V_p = V_{box} - V_w$, where V_{box} is the volume of the computational box. For complex configurations (e.g. several nanoparticles surrounded by water or within nanopores), the volume V_w can be estimated as $V_w = V_{out} - \sum_{p=1}^{N_p} V_p^{(p)}$, where $V_p^{(p)}$ and N_p are the volume of the $p-th$ particle and the total number of particles, respectively, whereas V_{out} is the volume of the surrounding space (i.e. $V_{out} = V_{box}$ for particles not loaded in nanopores, while $V_{out} = V_{pore}$ for cases where particles are loaded within a pore whose volume, computed by Equation 2.19, is V_{pore}). The use of Equation 2.19 relies upon the computation of the number density ρ_n. Using available packages in standard molecular dynamics software, an estimate of the average value for ρ_n can be easily computed after solvation of a dry geometry. Here, the overall water volume is estimated in a few realizations of each configuration of interest: several measures of ρ_n are collected and used to compute an average value and the corresponding standard deviation. The latter standard deviation generates uncertainties when computing the volume V_w, and consequently uncertainties of the scaling parameter (horizontal error bars in Figure 2.21). Alternative approaches based for instance on Monte-Carlo integration can be also used to calculate V_w accurately.

Finally, assuming θ as the sole, independent variable for D, all computed values relax within a narrow band around a linear curve (Figure 2.21) that can be readily described by the relationship

$$D(\theta) = D_B \left[1 + \left(\frac{D_C}{D_B} - 1 \right) \theta \right], \tag{2.20}$$

where D_B is the self-diffusion coefficient of bulk water, while D_C the self-diffusion coefficient of totally confined water. Remarkably, Figure 2.21 presents data from 58 different cases analyzed in this work as well as data available in the published literature. Here, despite the variety of the considered configurations, particles and sources of the results, a simple law is found to be sufficiently accurate to describe the phenomenon under study, thus confirming that θ is indeed an important controlling parameter under very diverse conditions and geometrical configurations. In order to have a more explicit formulation of Equation 2.20, details about the evaluation of D_C are provided in the next Section.

Note that, in Figure 2.21, results from the literature are also reported and compared with MD ones. First, by referring to the work of Milischuk *et al.* [179], the corresponding scaling parameters for the reported silica nanopores (with diameters 2, 3 and 4 nm) are computed. Second, the

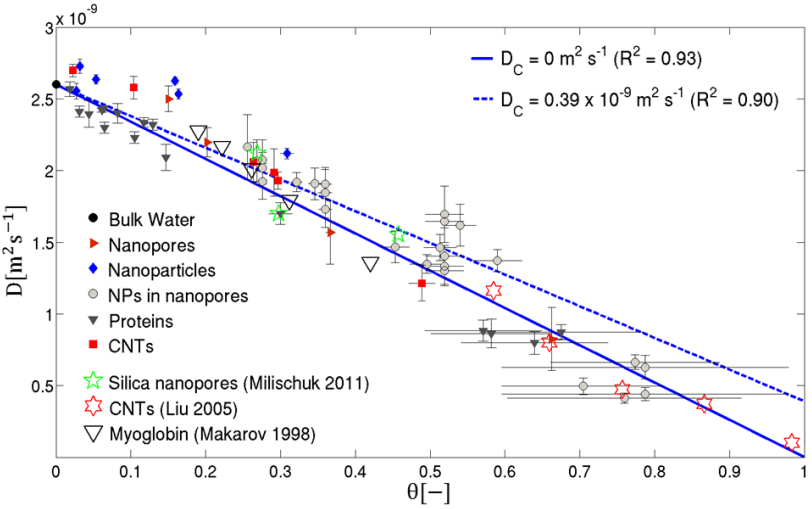

Figure 2.21.: Scaling behavior for the water diffusion coefficient D. The self-diffusion coefficient of water has been calculated for over 60 different cases, including spherical nanoparticles in water, water within nanopores with and without spherical nanoparticles, proteins and carbon nanotubes in water. 58 cases are the results of molecular dynamics simulations performed in this Chapter, under isothermal conditions. Results from the literature are also provided, for which the scaling variable θ is computed. The solid and the dashed lines represent Equation 2.20 for $D_C = 0$ and $D_C = 0.39 \times 10^{-9}$ m^2 s^{-1}, respectively. Equation 2.20 accurately recovers simulation and literature results with high coefficient of determination ($R^2 > 0.90$). The uncertainties on the value of D (vertical bars) refer to the fitting of the mean square displacement; whereas the uncertainties on the value of θ (horizontal bars) refer to the estimate of the total volume accessible to water molecules V_w. Figure adapted from Reference [27].

self-diffusivities evaluated by Liu *et al.* within five single walled carbon nanotubes (CNTs) are also reported in Figure 2.21 [180]. Finally, the results of water self-diffusivity around Myoglobin found by Makarov *et al.*

are also analyzed, and the corresponding scaling parameter θ estimated and reported in Figure 2.21 [181, 182]. Further details of those calculations are reported in Reference [27].

2.5. Thermodynamics insights

In this Section, the scaled results reported in Figure 2.21 are interpreted by a model based on experimental data of nanoconfined water.

Nanoconfined water shares some features with supercooled water, in that it may not crystallize upon cooling below the melting temperature of $T_M \approx 273.15$ K [17, 19]. Within the thin δ layer of water molecules next to a solid surface, the thermodynamic state depends on the characteristic confinement length scale, but only few experimental data are available [24]. In particular, the specific heat capacity c_p of nanoconfined water has been experimentally measured in narrow silica nanopores, and its variation with the temperature T is plotted in Figure 2.22a for a pore diameter of 1.7 nm [22]. This thermodynamic property depends on the diameter of the nanopore; however, for very small nanopores (i.e. < 1.7 nm), the heat capacity shows no meaningful peak, which suggests that no ice is present (effectively too far from the virtual LLCP because of the surface spreading pressure). In case of strong nanoconfinement, the heat capacity c_p seems to move gradually from a temperature-independent plateau, which starts at room temperature, to a linear function of the temperature, which is typical for ice, at very low temperature (i.e. <100 K). Using these experimental data and assuming $\theta \approx 1$ for such a strong nanoconfinement conditions, the energy variation associated with the transition from bulk to confined water can be readily computed as

$$\Delta h = -\int_{T}^{T_0} c_p dT = f\left(T\right), \tag{2.21}$$

with $f\left(T_0\right) = 0$ at the bulk water temperature $T_0 = 300$ K. From this, the inverse function $T = f^{-1}\left(\Delta h\right)$ can be derived as plotted in Figure 2.22b.

The volume occupied by the water molecules can be partitioned in two regions, the one with higher molecular mobility (B), coinciding with the bulk water, while the other with lower molecular mobility (C), including the confined molecules in the water boundary layer at the liquid-solid interface. Let h_B be the molar enthalpy of the bulk region and $h_C \leq h_B$

the molar enthalpy in the adsorbed region. Clearly, the energy variation associated with water nanoconfinement (i.e. energy of adsorption) can be written as

$$\Delta h = h_C - h_B \leq 0, \tag{2.22}$$

where h_B and h_C are the energy of bulk and confined water, respectively [25]. Since the confined region is typically limited to 1–2 layers of water molecules (for all the considered structures, $\delta < 0.6$ nm), it can be assumed that $\Delta h \approx -\varepsilon$, which is the minimum of the effective potential (U_{eff}) generated by the solid surface. The function f^{-1} can be used to compute the supercooled temperature of nanoconfined water corresponding to the energy variation $-\varepsilon$, that is to say $T = f^{-1}(-\varepsilon)$. In the work of Chen and colleagues [17], the diffusion coefficient of water molecules under strong nanoconfinement (i.e. within silica pores with diameter of 1.4 – 1.8 nm) is reported as a function of the temperature. From the latter experimental data, the diffusion coefficient of totally confined water D_C can be readily expressed in the form $D_C = D_B g'(T)$ (Figure 2.22c). Therefore, by combining the two sets of experimental data and knowing the value of ε, the diffusion coefficient of totally confined water D_C can be computed as

$$D_C/D_B = g'(T) = g'\left(f^{-1}(-\varepsilon)\right) = g(-\varepsilon). \tag{2.23}$$

The ratio D_C/D_B is plotted in Figure 2.22d for the different 58 cases analyzed here. For the iron oxide nanoparticles and carbon nanotubes, which are characterized by a fairly strong effective potential (large ε), $D_C \approx 0$. As the strength of the effective potential reduces, the value for the diffusion coefficient of totally confined water increases. However, even for the silica nanoparticles and nanopores, and for the proteins which are characterized by lower ε, in our computations D_C is at most 15% of D_B. We stress that the function $g(\Delta h)$ is a property of water, and here we have chosen to estimate it on the basis of measurements in silica nanopores only, because such experiments are among the very few that are well documented in literature.

In general, the volume of water can be partitioned into bulk (B) and confined (C). Invoking the mixing rule, the average diffusivity D of the

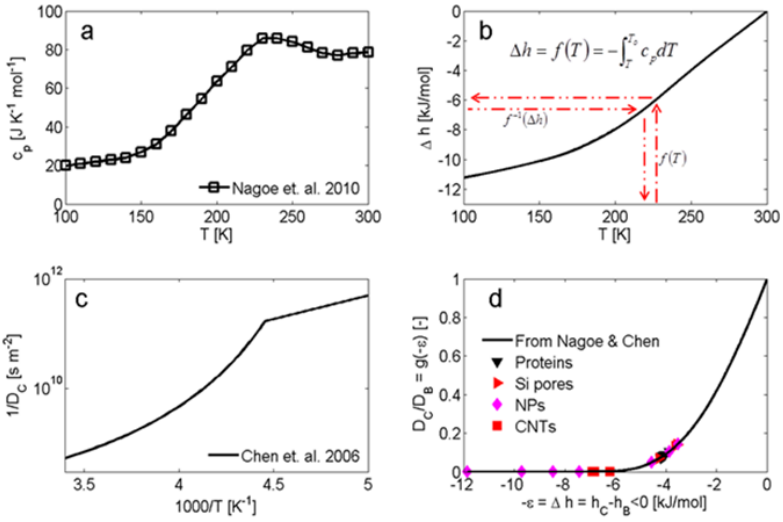

Figure 2.22.: Derivation of the function $D_C = g(-\varepsilon)$. (a) The specific heat capacity $c_p(T)$ of water confined in the narrowest silica pore reported in Nagoe *et al* [22]. (b) By integrating the latter function $c_p(T)$, the energy of nanoconfinement is evaluated as $\Delta h = f(T) = -\int_T^{T_0} c_p dT$. (c) The inverse function $T = f^{-1}(\Delta h)$ provides the temperature corresponding to a given energy Δh, hence it can be used in combination with the experimental results from Chen *et al.* where the diffusion coefficient (in narrow silica pores) is given as a function of T [17]. (d) The ratio between the diffusion D_C of fully confined water and the bulk diffusion D_C of water, $D_C/D_B = g(\Delta h)$, is reported and the corresponding values for all the considered configurations are shown, where $g(\Delta h) < 0.15$. Figure adapted from Reference [27].

system can be presented as

$$\begin{aligned} D &= \lim_{t\to\infty} \frac{1}{6t} \left\langle \left\| \overrightarrow{r_i}(t) - \overrightarrow{r_i}(0) \right\|^2 \right\rangle_{i\in V_B+V_C} = \\ &= \frac{1}{N_B+N_C} \lim_{t\to\infty} \frac{1}{6t} \sum_i^{N_B} \left\| \overrightarrow{r_i}(t) - \overrightarrow{r_i}(0) \right\|^2 + \\ &\quad + \frac{1}{N_B+N_C} \lim_{t\to\infty} \frac{1}{6t} \sum_i^{N_C} \left\| \overrightarrow{r_i}(t) - \overrightarrow{r_i}(0) \right\|^2 = \\ &= \left(1 - \frac{N_C}{N_B+N_C}\right) D_B + \frac{N_C}{N_B+N_C} D_C. \end{aligned} \tag{2.24}$$

where N_C and N_B are the number of water molecules in the confined and bulk regions, respectively. Considering that $N_C = \rho_C V_C / m_w$, being ρ_C the water (mean) density in the adsorbed region and m_w the mass of one water molecule, it follows:

$$D(\theta, \varepsilon) = D_B \left[1 + \left(\frac{D_C}{D_B} - 1 \right) \frac{\rho_C \theta}{\rho_C \theta + \rho_B (1 - \theta)} \right]. \tag{2.25}$$

Equation 2.25 is the fundamental one of the proposed model. Here, the average diffusivity for the considered volume depends on a geometrical parameter (θ) and an energetic parameter (ε). For the setups here considered, some simplifications are possible. First of all, the function

$$q_\iota = \frac{\rho_C \theta}{\rho_C \theta + \rho_B (1 - \theta)} = \frac{1 + \iota}{\iota + 1/\theta}, \tag{2.26}$$

with $\rho_C = (1 + \iota)\rho_B$, can be safely approximated as $q_\iota \approx \theta$ for the values of ρ_C of interest. In fact, here a maximum value for ι is observed to be: $\iota = 0.1 - 0.2$ (e.g. based on the density profile shown in Figure 2.16e for an SPIO particle), where the (average) value for ρ_C is computed by $\frac{\int_{r_0}^{r_0+\delta} \rho_C 4\pi r^2 dr}{\int_{r_0}^{r_0+\delta} 4\pi r^2 dr}$. In Figure 2.23 the exact function $q_\iota = \frac{1+\iota}{\iota+1/\theta}$ for two quite large values of ι ($\iota = 0.25$, $\iota = 0.5$) are shown. The negligible deviations between the above and the approximated function $q_\iota \approx \theta$ (even in such conservative cases) support the above simplifying assumption.

Therefore, Equation 2.25 degenerates into Equation 2.20, demonstrating that the diffusion of nanoconfined water can be interpreted invoking the thermodynamics of supercooled water. Moreover, based on the above discussion on D_C (see Figure 2.22d), for a large variety of nanoconfined systems the simplifying assumption $D_C/D_B \approx 0$ can be safely made. In such cases, the much simpler law

$$D(\theta, \varepsilon) \approx D(\theta) = D_B (1 - \theta) \tag{2.27}$$

is readily derived, showing the direct linear dependence of the water diffusion coefficient on the sole scaling parameter θ. Note that no empirical factor is needed to derive $D(\theta)$, with the latter law matching the values of the 58 MD simulations as well as 13 further configurations from the literature with a quite good coefficient of determination ($R^2 = 0.93$, solid line in Figure 2.21). The dashed line in Figure 2.21 represents, instead, Equation 2.20 with $D_C/D_B = 0.15$, corresponding to the largest value of D_C observed only in a few simulated cases (Figure 2.22d).

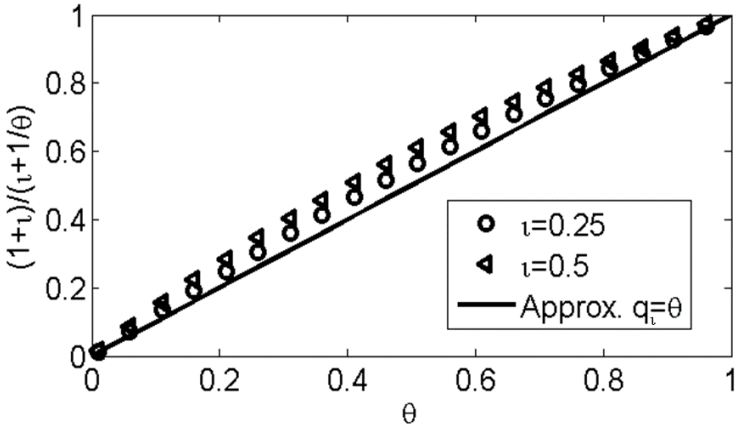

Figure 2.23.: Approximation of $q_\iota(\theta)$ function. The function $q_\iota(\theta) = \frac{1+\iota}{\iota+1/\theta}$ is plotted against the θ scaling variable at two (conservative / large) values of ι (symbols). The approximating function $q_\iota(\theta) = \theta$ (line) is also depicted.

2.6. Conclusions

In summary, the MD results and thermodynamics arguments reported in this Chapter show that the self-diffusion coefficient of nanoconfined water can be described by a unique dimensionless parameter θ, representing the ratio between the confined and total water volumes. The coefficient D scales linearly with θ and can be readily estimated, knowing the bulk (D_B) and totally confined (D_C) self-diffusion coefficient of water. This has been validated on the basis of almost sixty different cases and five different geometrical configurations, including the analysis of the water molecule dynamics within nanopores and carbon nanotubes, around nanoparticles and proteins. The coefficient of diffusion for totally confined water is quantified on the basis of the thermodynamics of supercooled water.

The proposed approach may be used to interpret experimental data collected in different scientific disciplines on the dynamics of water molecules under confined conditions, and to rationally design nanostructures for modulating the diffusion of water. This is of relevance in nanomedicine, nanotechnology as well as in more traditional engineering fields such as heat transport, fluid dynamics, and energy storage.

As an example, in Chapter 4 the $D(\theta)$ scaling law is exploited for proposing novel molecular sieves and sensors made out of carbon nanotube arrays, whereas in Chapter 6 the relaxivity enhancement encountered in case of nanoconfined contrast agents is successfully interpreted in the light of the scaling nature of self-diffusivity of nanoconfined water.